JOURNAL OF REINFORCED PLASTICS & COMPOSITES

Original article

Journal of Reinforced Plastics and Composites
2023, Vol. 42(7-8) 281–299

DOI: 10.1177/07316844221118633
journals.sagepub.com/home/jrp
SAGE

Failure behavior of laminated composite plates under anticlastic bending

Yakup O Alpay[1], Fatih E Oz[1,2], Fazil O Sonmez[1] and Kenan Cinar[1]

Abstract

In this study, the failure behavior of laminated composite plates subjected to anticlastic bending is investigated. Anticlastic bending is a special case of bi-axial out-of-plane loading that produces predominantly twisting moment. A test fixture is designed to actualize anticlastic loading condition. Carbon-fiber-reinforced epoxy composite is selected as the material of the specimens. Totally nine different layup configurations are chosen and at least four specimens are tested for each configuration. Acoustic emission monitoring (AEM) is utilized to detect the first-ply-failure load and the accumulation of damage in the laminates. In this method, elastic waves resulting from initiation and progression of damage are detected, and then AE signals are processed to identify the failure modes and determine the first-ply-failure load. A finite element model is developed to simulate the anticlastic bending test. A code is developed using ANSYS parametric design language to predict the first-ply-failure loads using various failure criteria like Tsai–Wu, Hashin, and Puck. The experimental and numerical results are then compared. Relative strengths and weaknesses of the failure criteria in estimating failure of laminated composite plates under anticlastic bending are discussed.

Keywords

laminated composites, multiaxial bending, testing, failure criteria, acoustic emission monitoring, finite elements analyses

Introduction

Laminated composite plates exhibit much more complex behavior than the conventional materials. Interactions between fibers and matrix; many different ways in which they may fail, for example, delamination, fiber breakage, matrix cracking, buckling of fibers, and debonding of fibers from matrix; predominance of a different failure mode over the others under a different loading state or a different layup pose great difficulty in predicting their failure behavior.

In industrial applications, designers face the difficulty of developing safe and optimal designs for composite parts under complex loading cases. So, understanding and predicting the failure behavior of the material under different loading conditions gain importance. Failure mechanisms and response of laminated plates are extensively studied and validity of the failure criteria is investigated for in-plane loading conditions.[1–9] On the other hand, not sufficient attention has been given to out-of-plane loading (i.e., transverse force, bending or twisting moments, or their combination). Many composite structural parts like aircraft wings and wind turbine blades are subjected to a combination of bending and twisting moments or transverse forces. Failure analyses of composites based on failure criteria validated only for in-plane loading cannot be considered reliable if the part is subjected to out-of-plane loads. Hence, reliable design of laminated composite parts requires use of failure theories validated for various loading conditions.

A number of researchers previously examined the intralaminar failure behavior of laminated composites under various out-of-plane loads and investigated the validity of different failure criteria. Irhirane et al.[10] compared the predictions of several static failure criteria for the first-ply and progressive failure of composite laminates under three-point bending with experimental results. Meng et al.[11] investigated the effects of lay-up configurations on the damage initiation under three-point bending. They compared the test results with the results of a 3D FEA model and an analytical model. Koc et al.[12] studied intralaminar failure behavior of CFRP specimens under four-point bending and compared the experimentally measured strengths with the

[1]Department of Mechanical Engineering, Bogazici University, Istanbul, Turkiye
[2]Composite Technologies Center of Excellence, Sabanci University-Kordsa, Istanbul Technology Development Zone, Istanbul, Turkey

Corresponding author:
Fazil O Sonmez, Department of Mechanical Engineering, Bogazici University, Istanbul, Bebek 34342, Turkiye.
Email: sonmezfa@boun.edu.tr

predictions of commonly used static failure theories like Tsai–Wu and Hashin.

In the literature, usually four-point-bending[12–15] or three-point-bending[11,13,16–23] tests conducted on composite specimens were considered to examine the validity of failure criteria for out-of-plane loads. In these tests, specimens were predominantly subjected to uniaxial bending, M_{xx} or M_{yy}. In the tests where transverse loads were applied,[24–26] specimens were predominantly under bi-axial bending (both M_{xx} and M_{yy}) as seen in Figure 1(a). On the other hand, in anticlastic loading, specimen is predominantly subjected to twisting moment, M_{xy}. This loading state is realized either by applying bending moments in opposite sense (Figure 1(b)) or by applying force couples having the same magnitude but opposite direction to the neighboring corners of a square plate as shown in Figure 1(c). If $M_{xx} = -M_{yy} = M_0$ and $x - y$ coordinate axes are rotated by 45° about z axis, the loading state on the plate will be $M_{x'x'} = M_{y'y'} = 0$ and $M_{x'y'} = M_0$ with respect to the new coordinate system $x' - y'$. Farshad et al.[27] used anticlastic bending to determine the shear modulus and Poisson's ratio of some polymers and foams. In another research, Farshad and Flüeler[28] investigated the mode III fracture toughness of various materials, including CFRP and GFRP, by means of anticlastic bending. Makeev et al.[29] used anti-clastic bending to assess the shear stress-strain curves in all three principal planes with a single experiment. Podczeck[30] used this method to determine the fracture properties of some pharmaceutical materials. Elmalich and Rabinovitch[31] used a high-order sandwich plate theory to study the twist behavior of soft-core sandwich plates with aluminum face sheets under anticlastic bending and compared the numerically and experimentally obtained values for the compliance. Goodsell et al.[32] developed an approximate elasticity solution for the response of composite laminates under anticlastic bending and their analytical solution agreed with the FE results for displacements and interlaminar shear stresses. However, anticlastic bending has not been used to investigate the failure behavior of composite materials in those studies.

In this study, the strength of continuous fiber-reinforced laminated composite plates with different stacking sequences are investigated under anticlastic bending and the validity of selected failure criteria is examined under this loading state. For this purpose, a new anticlastic bending test apparatus is designed (Figure 1(d)). Specimens with 100 mm × 100 mm dimensions, composed of 12 plies with various layup sequences are manufactured. The progressive failure behavior of the specimens is monitored during testing by means of acoustic emission monitoring (AEM). In this method, elastic waves resulting from initiation and accumulation of damage within the material are detected, and then the signal data are analyzed to identify the failure modes. The mechanical behavior of the specimens during the tests is simulated by a finite element model in ANSYS and a code is developed using ANSYS parametric design

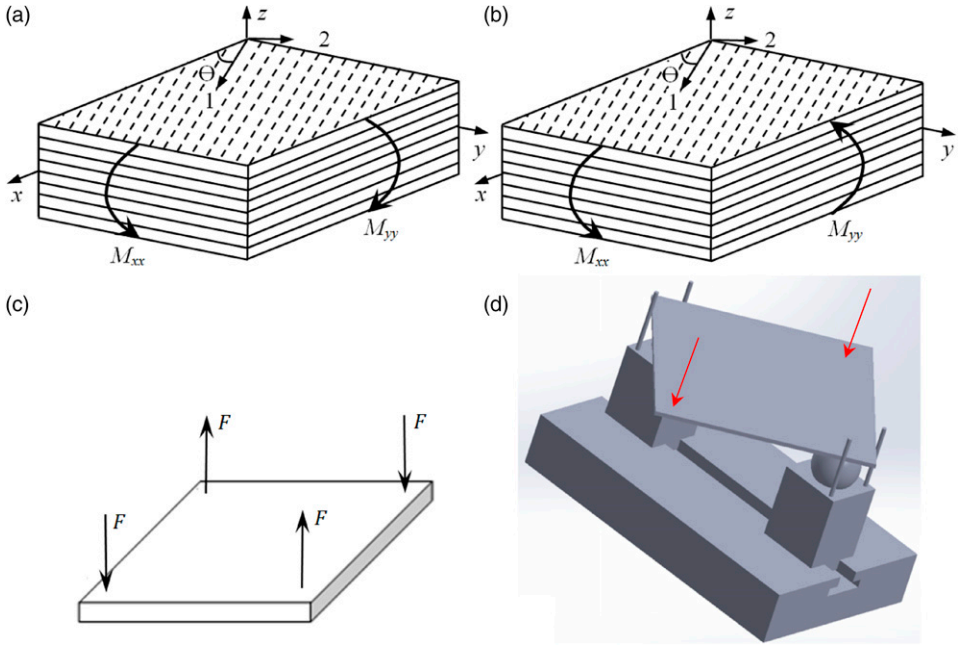

Figure 1. (a) Biaxial bending applied by two bending moments in the same sense; (b) Anticlastic bending applied by two bending moments in opposite sense; (c) Anticlastic bending applied by force couples; (d) Bottom portion of the anticlastic test setup developed in this study. The two forces are applied on the specimen by the upper half of the fixture (removed for clarity) which is identical to the bottom half.

language (APDL) to employ the selected failure criteria to predict the first-ply failure load levels, which are maximum stress, maximum strain, Tsai–Hill, Tsai–Wu, Hofman, Hashin, Puck, and quadric surfaces.[33] The experimental results and the predictions of the failure criteria are compared and the criteria that yield the most realistic results are determined for each stacking sequence. In this way, the validity of the chosen failure criteria is investigated for this type of loading condition and valuable information is provided for the designers as to the reliability of the failure criteria.

Experiments

Experimental set-up

As depicted in Figure 1(d), specimens are placed on two spherical steel supports, which hold the specimen at points on the diagonal close to the corners. Support points are 15 mm away from the intersecting edges and $15\sqrt{2}$ mm away from the corners. Pin inserts are used in the bottom fixture to ensure proper alignment of the specimens during testing. The prismatic supports are placed on a sliding base to accommodate different specimen sizes.

Material and specimen preparation

Composite plates are manufactured from AS4/8552 unidirectional composite prepregs. The fiber volume fraction of cured material is 57.4% according to the product data sheet.[34] The properties missing in the catalogue (v_{23}, S_{23}) are taken from reference.[35] Tables 1 and 2 present the material properties used in the FE model. Because laminae are transversely isotropic, one may assume the following equalities to hold: $Z_t = Y_t$, $Z_c = Y_c$, $S_{13} = S_{12}$, $v_{13} = v_{12}$, and $G_{23} = E_2/2(1 + v23)$. Nominal thickness of a ply is measured to be 0.184 mm.

First, prepregs are laid out on a steel tool with desired stacking sequence and thickness, vacuum bagged, and then cured in autoclave according to the manufacturer's recommended curing cycle.[36] The cured plates are cut into the shape of a square with 100 mm-length edges by using a water-cooled diamond disc. In order to observe how successfully the failure criteria predict the failure trend, that is, the change in the failure load with a change in the orientation angle, θ, unidirectional $[\theta_{12}]$, and symmetric angle-ply, $[(+\theta/-\theta)_3]_s$, layup configurations with increasing values of θ are chosen as listed in Table 3. Note that due to the symmetry in geometry and loading, $[\theta_{12}]$ and $[(90^\circ - \theta)_{12}]$, configurations and also $[(+\theta/-\theta)_3]_s$ and $[(90 + \theta/90 - \theta)_3]_s$ configurations yield the same result. Additionally, cross-ply configurations indicated in Table 3 are chosen. At least four specimens are tested for each configuration. In testing some configurations, especially unidirectional laminates, delamination is observed to occur before any intralaminar failure. Considering that the objective in this study is to examine the validity of intralaminar failure criteria under anticlastic bending, reinforcing strips with 20-mm width are bonded to the edges of the specimens as shown schematically in Figure 2 to reduce the delamination risk at the edges. The strips have two-ply thickness with 0° orientation angle. The centers of the circles in the figure indicate the loading points.

Table 1. Elastic properties of AS4/8552.[34]

E_1 (GPa)	E_2 (GPa)	G_{12} (GPa)	v_{12}	v_{23}
135.1	9.6	5.3	0.32	0.487

Table 2. Strength properties of AS4/8552.[34]

X_t (MPa)	X_c (MPa)	Y_t (MPa)	Y_c (MPa)	S_{12} (MPa)	S_{23} (MPa)
2137	−1531	63.9	−199.8	114.5	102.7

Table 3. Chosen layup sequences.

Unidirectional (UD)	Symmetric angle ply	Cross-ply (XP)
$[0_{12}]$	$[(5/-5)_3]_s$	$[(90/0)_3]_s$
$[5_{12}]$	$[(15/-15)_3]_s$	$[90_3/0_3]_s$
$[15_{12}]$	$[(30/-30)_3]_s$	
$[30_{12}]$	$[(45/-45)_3]_s$	
$[45_{12}]$		

Experimental procedure

Anticlastic bending tests. Anticlastic bending tests are performed on MTS servo-hydraulic test machine with displacement control, using the anticlastic bending fixture shown in Figure 3. The bottom and top portions of the fixture are attached to the testing machine via connectors. The upper part of the anticlastic fixture is rigidly attached to the stationary upper frame of the testing machine. Movement of the specimen in the x and y directions is prevented during testing by means of the pins as shown in Figures 1(d) and 3. The bottom part of the fixture is attached to the piston, which is moved upward with a speed of 1.8 mm/min to ensure the loading is quasi static. The load is increased until the specimen breaks apart so that the ultimate load level can be determined. Rubber bands are placed between the balls and the specimen to reduce stress concentration at the points of application of loads and eliminate AE signals that might arise due to sliding between the balls and the specimens. Two piezoelectric transducers are symmetrically placed on the specimen to detect acoustic emission signals. Before placing the transducers on the specimen, the surface of the specimen is cleaned and ultrasonic gel is applied on both surfaces for smooth transmission of the acoustic waves. The gel layer serves as a coupling agent between the sensor

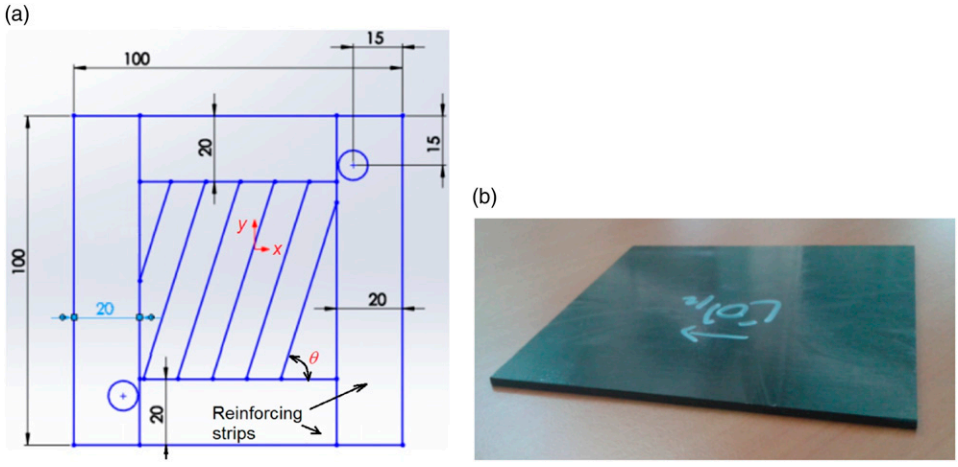

Figure 2. (a) Schematic of the specimen and the loading points, (b) A picture of a specimen without strips.

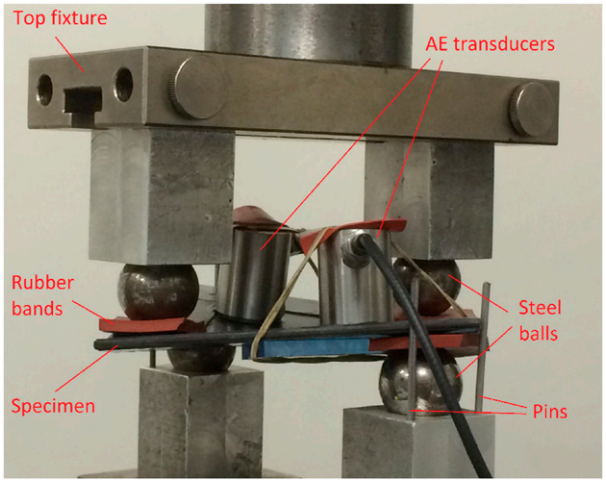

Figure 3. The test apparatus and AE sensors.

surface and the specimen by creating a continuous medium between them. In order to prevent sliding of the transducers during testing, which may produce noise signals, they are secured by means of elastic bands and tapes. The acoustic emission system starts before the bending test and stops at the same time. The data collected by the acoustic emission device and the test equipment are synchronized after the test by taking the time at the end of the test as the reference time.

Acoustic emission monitoring (AEM). It is not easy to determine the first-ply failure load for composite materials experimentally unless the first and final-failure load levels are the same. This is because initiation of damage usually does not result in an appreciable change in macro behavior of composites. Even in coupon tests under tension, a laminate may not suddenly fail throughout the specimen, damage may gradually accumulate, and thus a drop or a significant change in the slope of the load–displacement curve may not happen. The question is how extensive the initial damage should be to consider the first-ply failure to have occurred. Fortunately, AEM provides an effective tool for detecting the first-ply failure, progression and accumulation of damage, and even the failure mode. Different failure mechanisms generate characteristic AE signals. It is possible to figure out the failure mode by examining AE signals.

In this study, a two-channel MISTRAS AE system is used with PK15I type piezoelectric sensors. Its resonance frequency and operating frequency range are 150 kHz and 100–450 kHz, respectively. This frequency range is more suitable for detecting damage associated with matrix dominated failure modes. PAC AEwin^{TM} software is used for the acquisition of AE data. Peak definition time, hit definition time, and hit lockout time are selected as 50, 100, and 300 microseconds, respectively. The sampling rate is selected as five mega samples per second. In order to eliminate background noise 55 dB threshold is selected during testing. Only the signals recorded with an amplitude greater than 55 dB are recorded as hit data. A fast Fourier transform (FFT) analysis is carried out to examine the signals in the frequency domain. Acoustic emission system produces signals characterized by eight AE features: Peak amplitude, peak frequency, rise time, counts, duration, energy, absolute energy, and signal strength. Peak frequency is the frequency of the peak amplitude of a hit. Energy parameter is the time integral of the absolute signal voltage.[37] Its magnitude depends on the value of energy reference gain, which is selected as 20 dB. The energy parameter is without unit, but it is expressed as "eu," which stands for "energy unit" in AEWin PAC software.

Determination of the first-ply-failure load. In-situ observation techniques, like edge microscopy and digital image correlation (DIC) provided evidence for the correlation between AE parameters and failure modes.[38–40] Correlation of

AE signals with damage modes has been the subject of many studies.[38–46] Some of them[41–43] attempted to identify the failure modes of composite materials by associating each failure mode with a different range of peak frequency. However, different peak frequency bands may be observed when a single damage mode occurs as revealed by Baker et al.[45] It was reported that different peak frequency values were recorded with wideband AE sensors when matrix cracking occurred in 90° plies of a cross-ply laminate. For this reason, identification of failure modes based on just frequency content is not reliable.

In this study, the test fixture and the load condition do not permit use of in-situ optical tools, such as DIC or edge microscopy to correlate AE signals with failure modes. In order to determine the first-ply failure load and provide a reliable correlation between the AE parameters and the failure modes, several AE parameters are considered together with the load–displacement curves. Besides, sudden changes in the cumulative number of registered signals and formation of new frequency bands are attributed to initiation and progression of a failure mechanism. Effectiveness of this method was previously seen for tension and three-point bending tests of glass-fiber reinforced composites.[46]

Determination of delamination. The first-ply failure may be due to intralaminar failure or delamination failure depending on the loading, layup sequence, and material. In this study, the validity of intralaminar failure criteria under anticlastic bending is investigated. For this reason, it is important that the first-ply failure is due to intralaminar failure mode not delamination. In order to delay delamination, strips are glued to the edges. Besides, the load level at which delamination occurs is determined to see whether the first ply-failure mode is delamination or not. The delamination failure load is first determined based on the experimental data. Previous studies on different composite specimens under tensile loading[38–40] and flexural loading[46–48] revealed that acoustic emission data provided important evidences for determining various failure modes including delamination failure. The results of these studies showed that geometry, material, layup sequence, and sensor types affected the values of AE parameters of the failure modes but a significant conclusion was that a large-scale delamination between plies caused significant load drops in load–displacement curves and also initiation of new AE clusters or groups or a stop in the recording of AE clusters or groups. A small scale debonding that does not grow with increasing load does not show such indications, but it cannot be considered as a delamination failure. This approach is used in this study to determine the delamination failure under anticlastic loading.

Secondly, delamination is checked using the delamination model of Christensen and DeTeresa.[49] According to the model, delamination is predicted if the following inequality is satisfied

$$\frac{\sigma_{33}}{S_{T3}} + \frac{\tau_{31}^2 + \tau_{32}^2}{S_{IL}} \geq 1 \quad (1)$$

where σ_{33} is out-of-plane normal stress, τ_{31} and τ_{32} are out-of-plane shear components of stress, S_{T3} is the tensile strength in the thickness direction, and S_{IL} is the interlaminar shear strength. Solid elements are used in the finite element model. For this reason, out-of-plane stress components can be obtained after the finite element analysis. The strength values in the thickness direction are provided in references [50] and [51], which are $S_{T3} = 29.3$ MPa and $S_{IL} = 65$ MPa.

Finite elements analyses (FEA)

A finite element model is developed to simulate the anticlastic bending test and determine the stress and strain states within the specimen using commercial FEA analysis program ANSYS. A code is developed in ANSYS Parametric Design Language (APDL) to implement the failure criteria and predict the first-ply-failure load.

SOLID185, a layered 3D structural solid element defined by eight nodes, is used to mesh the structural volume (Figure 4). The element has three degrees of freedom at each node. Shell element could be used, but solid element type is preferred in order to obtain 3D stress and strain states and apply 3D formulations of the failure criteria. The material is assumed to behave linearly elastic until first-ply failure occurs. Since the tests are conducted under displacement control, displacement boundary conditions are defined in the FE model. Considering that the upper fixture is rigidly fixed to the upper frame of the testing machine and the lower fixture attached to the piston is moved slowly upward, the two nodes where the upper supports touch are held in the same position in the transverse (z-) direction (Figure 4). The two nodes on the same diagonal where the bottom supports touch are given a predetermined displacement in the transverse (z-) direction. In order to prevent rigid body motion of the FE model in other degrees of freedom, three nodes are selected close to the middle of the specimen and they are held in the x and y directions.

The magnitudes for the material strength and stiffness in Tables 1 and 2 are used in the FE model. In order to determine the first-ply failure load level, the value of the applied displacement for which the maximum failure index becomes equal to 1.0 is iteratively found using the secant algorithm. In this method, the maximum failure index values, f_1 and f_2, corresponding to two arbitrary displacements applied to two opposite corner locations (Figure 2(a)) are numerically calculated. The maximum failure index, f, is considered as a function of the applied displacement, δ. The root of function $(f(\delta) - 1)$ is

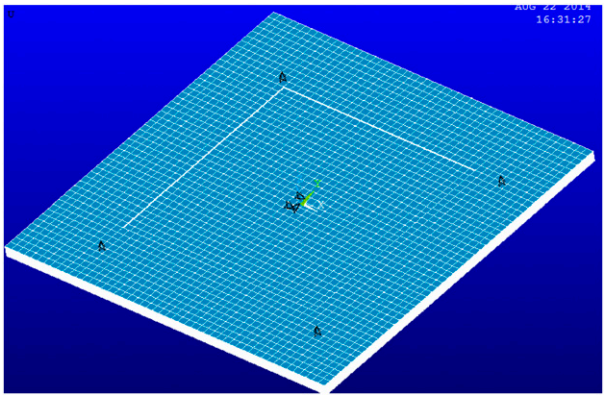

Figure 4. The meshed structural model of the specimen.

iteratively found using secant algorithm. After obtaining convergence, that is, finding the applied displacement such that the maximum failure index is equal to 1.0 ($f = 1.0$), the corresponding stress and strain states, the deflections, the reaction forces (i.e., the failure load), are extracted from the FE results.

Because the concentrated forces and the sharp edges between the strips and the laminate in the FE model cause stress concentrations more severe than the actual case, these regions are not considered in the failure analysis. Convergence analyses are performed to determine the optimum mesh size. Three different element sizes, 1.0 mm, 2.0 mm, and 4.0 mm, are tried, and the differences in the results indicate that the suitable mesh size is 2.0 mm. Thickness is divided by the number of plies. Accordingly, each element has thickness equal to 0.184 mm. Then, there are 16 elements in the thickness direction in the region with strips and 12 elements in the region without strips. The total number of elements is 36,400.

Intralaminar failure criteria

Maximum stress,[52] maximum strain,[52] Hashin,[53] Tsai–Wu,[54] Puck,[56] Tsai–Hill,[52] Hoffman,[57] and quadric surfaces[58] failure criteria are used to predict the failure load and the corresponding deflection. Among these, the first five criteria are defined in ANSYS software; the rest is implemented by developing codes. In the following, the expressions for the failure criteria are given in terms of the stress or strain components in the material coordinates, σ_i, τ_{ij}, ε_i, and ε_{ij}. 3D forms of the failure criteria are used to calculate the failure index, f. If the maximum value of the failure index in the laminate exceeds 1.0, failure is predicted.

Tsai–Wu failure criterion[54] is a non-linear stress-based criterion that accounts for interaction between normal stress components; however, it does not predict the failure mode. It includes quadratic as well as linear terms

$$f = \frac{\sigma_1^2}{X_t|X_c|} + \frac{\sigma_2^2}{Y_t|Y_c|} + \frac{\sigma_3^2}{Z_t|Z_c|} + \frac{\tau_{12}^2}{S_{12}^2} + \frac{\tau_{13}^2}{S_{13}^2} + \frac{\tau_{23}^2}{S_{23}^2} - \frac{\sigma_1\sigma_2}{\sqrt{X_tX_cY_tY_c}} - \frac{\sigma_1\sigma_3}{\sqrt{X_tX_cZ_tZ_c}} - \frac{\sigma_2\sigma_3}{\sqrt{Y_tY_cZ_tZ_c}} + \sigma_1\left(\frac{1}{X_t} + \frac{1}{X_c}\right) + \sigma_2\left(\frac{1}{Y_t} + \frac{1}{Y_c}\right) + \sigma_3\left(\frac{1}{Z_t} + \frac{1}{Z_c}\right) \tag{2}$$

where X_t, X_c, Y_t, Y_c, Z_t, Z_c, S_{12}, S_{13}, and S_{23} are the strength values in the material coordinates. Their values are given in Section 2.2.

Hoffman criterion[57] is a nonlinear stress-based criterion accounting for stress interaction, but it does not predict the failure mode. It includes quadratic as well as linear terms. Only the coefficients of the interaction terms are different from that of Tsai–Wu criterion

$$f = \frac{\sigma_1^2}{X_t|X_c|} + \frac{\sigma_2^2}{Y_t|Y_c|} + \frac{\sigma_3^2}{Z_t|Z_c|} + \frac{\tau_{12}^2}{S_{12}^2} + \frac{\tau_{13}^2}{S_{13}^2} + \frac{\tau_{23}^2}{S_{23}^2} + \sigma_1\sigma_2\left(\frac{1}{X_tX_c} + \frac{1}{Y_tY_c} - \frac{1}{Z_tZ_c}\right) + \sigma_1\sigma_3\left(\frac{1}{X_tX_c} - \frac{1}{Y_tY_c} + \frac{1}{Z_tZ_c}\right) + \sigma_2\sigma_3\left(-\frac{1}{X_tX_c} + \frac{1}{Y_tY_c} + \frac{1}{Z_tZ_c}\right) + \sigma_1\left(\frac{1}{X_t} + \frac{1}{X_c}\right) + \sigma_2\left(\frac{1}{Y_t} + \frac{1}{Y_c}\right) + \sigma_3\left(\frac{1}{Z_t} + \frac{1}{Z_c}\right) \tag{3}$$

Tsai–Hill[52] is a non-linear stress-based criterion that accounts for stress interaction; however, it does not predict failure mode. It only includes quadratic terms. It does not assume any effect of the difference in tensile and compressive strengths as opposed to Tsai–Wu and Hoffman criteria, hence the linear terms disappear

$$f = \frac{\sigma_1^2}{X^2} + \frac{\sigma_2^2}{Y^2} + \frac{\sigma_3^2}{Z^2} + \frac{\tau_{12}^2}{S_{12}^2} + \frac{\tau_{13}^2}{S_{13}^2} + \frac{\tau_{23}^2}{S_{23}^2} - \sigma_1\sigma_2\left(\frac{1}{X^2} + \frac{1}{Y^2} - \frac{1}{Z^2}\right) - \sigma_1\sigma_3\left(\frac{1}{X^2} - \frac{1}{Y^2} + \frac{1}{Z^2}\right) - \sigma_2\sigma_3\left(-\frac{1}{X^2} + \frac{1}{Y^2} + \frac{1}{Z^2}\right) \tag{4}$$

Here, X, Y, and Z denote either tensile or compressive strength depending on the sign of σ_1, σ_2, and σ_3, respectively.

The quadric surfaces criterion[58] is a non-linear stress-based criterion. It not only accounts for stress interaction between normal stress components, but also between normal and shear stress components. It also includes the linear terms of the shear stress components. Failure

indices, f_{ij}, are calculated for 1–2, 2–3, and 1–3 planes and the maximum of these is taken as the failure index $f = \max(f_{12}, f_{13}, f_{23})$

$$f_{12} = \frac{a}{X^2}\sigma_1^2 + \frac{a}{Y^2}\sigma_2^2 + \frac{a}{S_{12}^2}\tau_{12}^2 + \frac{b}{XY}\sigma_1\sigma_2 + \frac{b}{XS_{12}}\sigma_1|\tau_{12}| + \frac{b}{YS_{12}}\sigma_2|\tau_{12}| + \frac{c}{X}\sigma_1 + \frac{c}{Y}\sigma_2 + \frac{c}{S_{12}}|\tau_{12}|$$

$$f_{23} = \frac{a}{Y^2}\sigma_2^2 + \frac{a}{Z^2}\sigma_3^2 + \frac{a}{S_{23}^2}\tau_{23}^2 + \frac{b}{YZ}\sigma_2\sigma_3 + \frac{b}{YS_{23}}\sigma_2|\tau_{23}| + \frac{b}{ZS_{23}}\sigma_3|\tau_{23}| + \frac{c}{Y}\sigma_2 + \frac{c}{Z}\sigma_3 + \frac{c}{S_{23}}|\tau_{23}|$$

$$f_{13} = \frac{a}{X^2}\sigma_1^2 + \frac{a}{Z^2}\sigma_3^2 + \frac{a}{S_{13}^2}\tau_{13}^2 + \frac{b}{XZ}\sigma_1\sigma_3 + \frac{b}{XS_{13}}\sigma_1|\tau_{13}| + \frac{b}{ZS_{13}}\sigma_3|\tau_{13}| + \frac{c}{X}\sigma_1 + \frac{c}{Z}\sigma_3 + \frac{c}{S_{13}}|\tau_{13}| \quad (5)$$

where a = 0.98, b = 0.49, and c = 0.02,[58] which are found by employing stability conditions and enforcing satisfaction of the equations for special loading cases like $a + c = 1$ for $\sigma_{11} = X$, $\sigma_{22} = \tau_{12} = 0$. X, Y, and Z denote either tensile or compressive strength depending on the sign of σ_1, σ_2, and σ_3, respectively.

The maximum stress criterion[52] is linear and stress based. It can predict the failure mode. It does not account for stress interaction. This criterion states that failure occurs if one of the following conditions is satisfied

$$\sigma_1 \geq X_t \text{ or } \sigma_1 \leq X_c \text{ or } \sigma_2 \geq Y_t \text{ or } \sigma_2 \leq Y_c \text{ or } \sigma_3 \geq Z_t \text{ or } \sigma_3 \leq Z_c \text{ or } |\tau_{12}| \geq S_{12} \text{ or } |\tau_{13}| \geq S_{13} \text{ or } |\tau_{23}| \geq S_{23} \quad (6)$$

The maximum strain criterion[52] is linear and strain based. It can predict the failure mode. It does not account for interaction between strain components. This criterion states that failure occurs if one of the following conditions is satisfied

$$\varepsilon_1 \geq X_{\varepsilon t} \text{ or } \varepsilon_1 \leq X_{\varepsilon c} \text{ or } \varepsilon_2 \geq Y_{\varepsilon t} \text{ or } \varepsilon_2 \leq Y_{\varepsilon c} \text{ or } \varepsilon_3 \geq Z_{\varepsilon t} \text{ or } \varepsilon_3 \leq Z_{\varepsilon c} \text{ or } |\varepsilon_{12}| \geq S_{\varepsilon 12} \text{ or } |\tau_{13}| \geq S_{\varepsilon 13} \text{ or } |\tau_{23}| \geq S_{\varepsilon 23} \quad (7)$$

where $X_{\varepsilon t}$, $X_{\varepsilon c}$, $Y_{\varepsilon t}$, $Y_{\varepsilon c}$, $Z_{\varepsilon t}$, and $Z_{\varepsilon c}$ are the maximum allowable tensile and compressive strains in the 1, 2, and 3 directions, respectively, $S_{\varepsilon ij}$ is the maximum allowable shear strain in the $i-j$ plane.

Hashin criterion[53] is a nonlinear and physically based failure criterion, which can predict the failure mode. It also accounts for stress interaction. Hashin criterion predicts failure if one of the following conditions is satisfied

$$\left(\frac{\sigma_1}{X_t}\right)^2 + \frac{\tau_{12}^2 + \tau_{13}^2}{S_{12}^2} \geq 1 \quad \text{if} \quad \sigma_1 \geq 0$$
$$\frac{\sigma_1}{X_c} \geq 1 \quad \text{if} \quad \sigma_1 < 0$$
$$\left(\frac{\sigma_2 + \sigma_3}{Y_t}\right)^2 + \frac{\tau_{12}^2 + \tau_{13}^2}{S_{12}^2} + \frac{\tau_{23}^2 - \sigma_2\sigma_3}{S_{23}^2} \geq 1 \quad \text{if} \quad \sigma_2 + \sigma_3 \geq 0$$
$$\left(\frac{\sigma_2 + \sigma_3}{2S_{23}}\right)^2 + \frac{\tau_{12}^2 + \tau_{13}^2}{S_{12}^2} + \left[\left(\frac{Y_c}{2S_{23}}\right)^2 - 1\right]\frac{\sigma_2 + \sigma_3}{|Y_c|} + \frac{\tau_{23}^2 - \sigma_2\sigma_3}{S_{23}^2} \geq 1 \quad \text{if} \quad \sigma_2 + \sigma_3 < 0 \quad (8)$$

Puck et al.[55,56] consider two failure types, one is fiber failure and the other is inter-fiber failure (matrix cracking). In the simple version,[59] the criterion for fiber failure is like the maximum stress criterion. Fiber failure occurs if

$$\sigma_1 \geq X_t \quad \text{or} \quad \sigma_1 \leq X_c \quad (9)$$

Puck criterion distinguishes three different modes for inter-fiber failure. According to the criterion, a fracture with 0° angle (mode A) occurs if the transverse stress, σ_2, is tensile and the following condition is satisfied

$$\sqrt{\left(\frac{\tau_{12}}{S_{12}}\right)^2 + \left(1 - p_\perp^{(+)}\frac{Y_t}{S_{12}}\right)^2\left(\frac{\sigma_2}{Y_t}\right)^2} + p_\perp^{(+)}\frac{\sigma_2}{S_{12}} \geq 1 \quad \text{if} \quad \sigma_2 \geq 0 \quad (10)$$

Mode B fracture occurs under a compressive transverse normal stress, σ_2, and shear stress in the 1–2 plane, τ_{12}, if the following condition is satisfied

$$\frac{1}{S_{12}}\left(\sqrt{\tau_{12}^2 + \left(p_\perp^{(-)}\sigma_2\right)^2} + p_\perp^{(-)}\sigma_2\right) \geq 1 \quad \text{if} \quad \sigma_2 < 0 \quad \text{and} \quad \left|\frac{\sigma_2}{S_{12}}\right| \leq \frac{R_{\perp\perp}^A}{|\tau_{12c}|} \quad (11)$$

Mode C fracture occurs under a compressive transverse normal stress, σ_2, and shear stress in the 1–2 plane, τ_{12}, which is large enough to cause fracture in an oblique plane, if the following condition is satisfied

$$\left[\left(\frac{\tau_{12}}{2\left(1 + p_{\perp\perp}^{(-)}S_{12}\right)}\right)^2 + \left(\frac{\sigma_2}{Y_c}\right)^2\right]\frac{Y_c}{|\sigma_2|} \geq 1 \quad \text{if} \quad \sigma_2 < 0 \quad \text{and} \quad \left|\frac{\tau_{12}}{\sigma_2}\right| \leq \frac{|\tau_{12c}|}{R_{\perp\perp}^A} \quad (12)$$

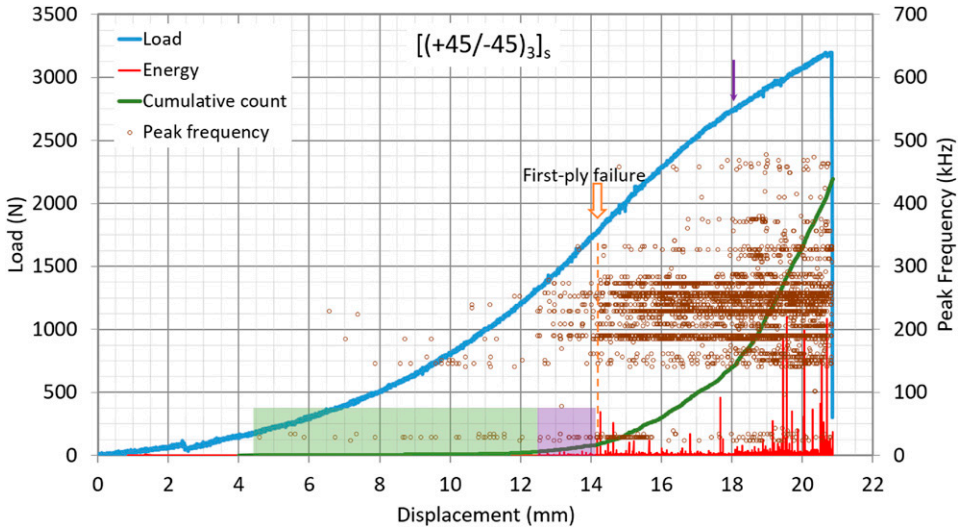

Figure 5. Test results for $[(45/-45)_3]_s$, laminate with no strips. The low-energy signals in the green and purple regions are attributed to micro damage. Occurrence of a high-energy signal and subsequent high-energy signals, start of high-density frequency bands, and increase in the slope of the cumulative curve indicate first-ply failure at the load level of 1770 N. The purple arrow shows another ply-failure mechanism where new frequency bands form and the slope of the load–displacement and cumulative curve changes.

The inclination parameters of Puck's model are taken as $p_{\perp}^{(+)} = 0.35$, $p_{\perp}^{(-)} = 0.3$, $p_{\perp\perp}^{(-)} = 0.25$, and $p_{\perp\parallel}^{(+)} = 0.25$ as suggested for carbon fiber/epoxy by Puck et al.[56]. The other parameters can be found from

$$R_{\perp\perp}^{A} = S_{12}\frac{p_{\perp\perp}^{(-)}}{p_{\perp}^{(-)}} \quad \tau_{12c} = S_{12}\sqrt{1 + 2p_{\perp\perp}^{(-)}} \tag{13}$$

3D formulations of Puck criterion are given in references [56] and [59].

Results and discussion

Experimental results

First, plates with and without reinforcing strips are tested and the results are compared in order to distinguish the AE characteristics of damage in strips.

Figure 5 shows load & energy & frequency versus displacement graphs for a specimen with $[(45/-45)_3]_s$ layup configuration with no strips. The displacement in the graphs is the displacement of the piston attached to the lower fixture shown in Figure 3. As mentioned before, the energy parameter is without unit. Energy level depends on the type and extent of damage and also on the distance between the transducers and the location of damaged region. Moreover, it depends on the energy reference gain, which is chosen to be 20 dB. In this study, relative magnitude of the energy parameter, not its absolute magnitude, is used to get information on initiation and accumulation of damage. For these reasons, the magnitude of the energy is not shown in the figure and it is scaled to fit the graphical region. The cumulative count, which is the sum of the number of counts for each acoustic event, is also shown in the figure. Again, the shape of the graph, not the absolute number of hits, is used to reach conclusions on initiation of damage. Accordingly, this curve is also scaled to fit the figure.

The initial portion of the load–displacement curve up to 1400 N is nonlinear with increasing stiffness because of the rubber bands. The subsequent linear part of the curve represents the actual stiffness of the specimen. The highlighted green region in the figure indicates noise signals that may arise due to sliding of transducers or background noise of the servo-hydraulic test machine. Since the dimensions of the AE transducers are not sufficiently small for the tested specimens and significant curvature develops in the thin specimens before failure, it is not possible to eliminate the noise signals due to sliding of the transducers. Just after the signals, highlighted in green region, are detected, energy levels of the recorded signals increase a little bit and different peak frequency values are activated. This is most likely due to matrix micro cracking within the plate. In this study, occurrence of localized damage is not considered as a ply failure. If damage initiates at a given load level and progresses with an increase in load, then it is considered as first-ply failure. In the green region, however, no increase in the slope of the cumulative curve, no increase in the density of the frequency bands (increased rate of AE hits at certain frequencies), no subsequent high-energy peaks are observed. For these reasons, there is no progression of localized damage. On the other hand, at 1770 N, a signal is detected with a much higher energy level. The density of the AE signals increases after the first-ply failure indicating progression of the damage; besides energy levels of the

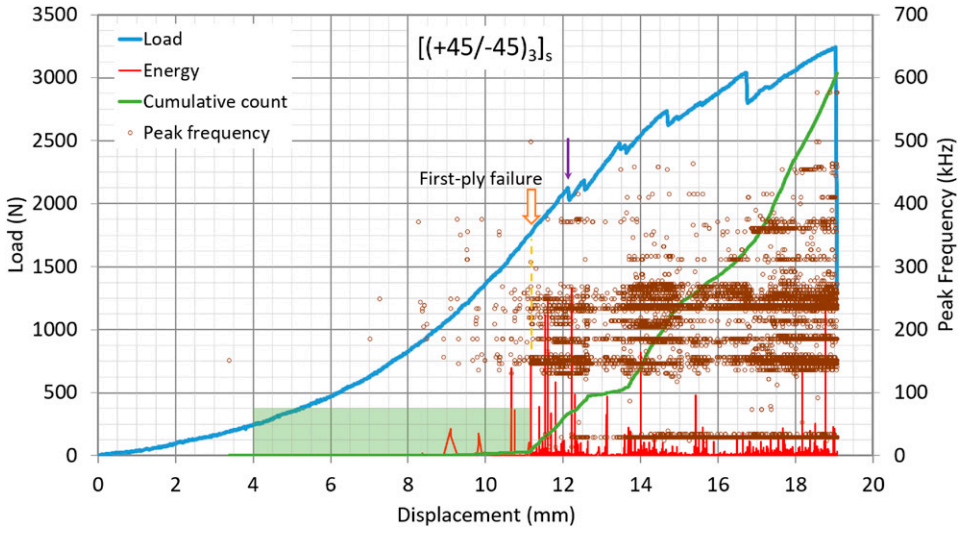

Figure 6. Test results for $[(45/-45)_3]_s$ laminate with strips. The low-energy signals in the green region are attributed to micro cracking. At 1750 N, initiation of high-density frequency bands and associated significant increase in the slope of the cumulative count, and subsequent high-energy signals indicate first-ply failure. The drop in the load level at 2100 N, which is associated with a very high-energy signal, is attributed to separation of the reinforcing strips from the main laminate.

signals become higher and the slope of the cumulative count curve increases. These imply accumulation of damage. Hence, 1770 N is considered as the first-ply failure load for this plate. In the later stages of loading, new frequency bands form, which indicates activation of different failure mechanisms.[41–43] This can clearly be seen after 2750 N. It can be assumed to be due to breaking of some fibers. Because there is no load drop before the final failure, there is no indication of delamination failure.

Test results for $[(45/-45)_3]_s$ laminate with strips can be seen in Figure 6. This is the same configuration as the one shown in Figure 5, but with reinforcing strips. Because AE signals due to cracking of the adhesive bond between the reinforcing strips and the laminate are also recorded during this test, there are differences in AE characteristics compared to the laminate with no strips. The first-ply failure level of $[(45/-45)_3]_s$ laminate with strips is expected to be equal to or higher than that of the laminate with no strips. There are some high-energy values in the region shown with green color in Figure 6, but these are followed by high-energy signals. At 1750 N, the density of the peak frequency values between 150 and 270 kHz increases drastically and the cumulative count shows significant increase in slope. One may assume that damage occurs within the laminate not at the reinforcing strip at this load level considering the similarities to the behavior of the unreinforced laminate shown in Figure 5. The failure mode is matrix cracking in the transverse direction as in the previous specimen. Otherwise, extensive fiber breakage or delamination would have caused significant degradation in stiffness. The first-ply failure load level does not change with the reinforcing strips for this layup; only the corresponding displacement is smaller because of the stiffening effect of the strips. One may conclude that the first-ply failure mode for this layup configuration without strips is already intralaminar failure not delamination. After first-ply failure occurs, the highest AE energy value is observed at 2100 N with a drop in the load level. At this stage, some reinforcing strips can be assumed to be separated from the laminate, because no load drop is observed in the other specimen with no strips (Figure 5) and debonding in the reinforcing strips were visible in intermediate stages of the test. By the end of the test, significant portion of the strips becomes separated from the laminate; for this reason, the final failure load is about the same as that of the specimen with no strips.

The test results for specimens having $[(5/-5)_3]_s$, $[(15/-15)_3]_s$, and $[(30/-30)_3]_s$ layup configurations with strips are given in Figure 7. For the specimen with $[(5/-5)_3]_s$ layup, one may assume that the first-ply failure initiates with a sudden drop at 630 N. With this drop, three different peak frequency bands are subsequently activated. These are considered as evidences of delamination. Previously activated frequency bands are not associated with high-energy signals. For the laminate with $[(15/-15)_3]_s$ layup, at load level 760 N, a high-energy signal is detected (shown by purple arrow). However, no subsequent progression of damage occurs, since the slope of the cumulative curve does not increase and subsequent energy levels are low. For these reasons, this is not taken as the first-ply failure load. At load level 990 N, a signal with a high energy is detected. Subsequently, high-energy signals are continued to be generated and the slope of the cumulative curve shows a significant increase. Accordingly, the first-ply failure load is taken to be 990 N. The previous signals may be due to

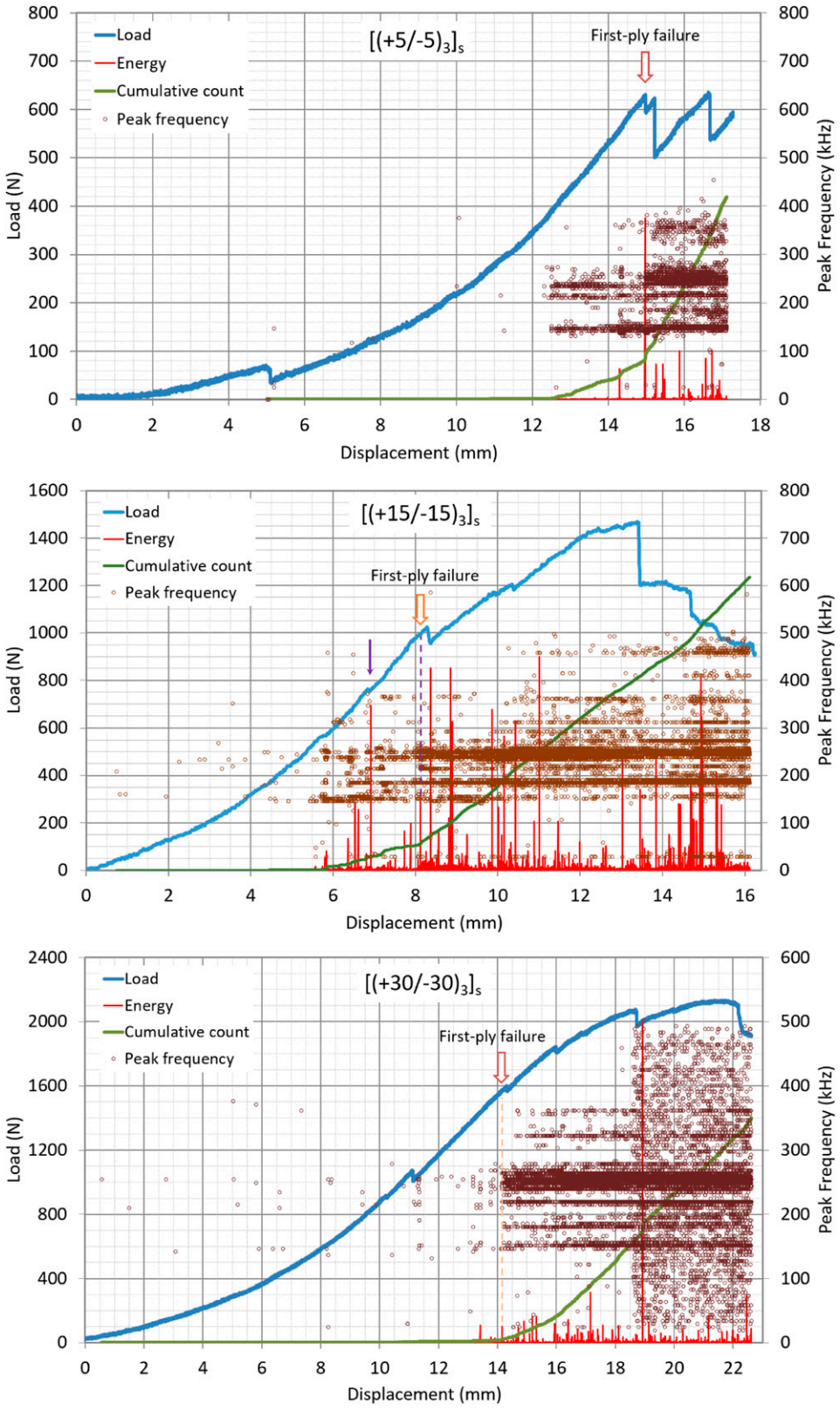

Figure 7. Test results for $[(5/-5)_3]_s$, $[(15/-15)_3]_s$, and $[(30/-30)_3]_s$ laminates with strips.

noises arising from sliding of AE transducers, development of micro cracks, local damage that does not progress, or partial debonding between the laminate and the strips. The large sudden drop at 1465 N and the initiation of a new peak frequency band around 460 kHz are attributed to delamination failure in the main laminate. For the $[(30/-30)_3]_s$ laminate, a load drop occurs at 1580 N, a number of frequency bands are activated, and signals continue to be recorded until failure with increased density as the cumulative curve indicates. Subsequent high-energy signals imply that damage induced at this load level progresses. Above this load level, stiffness gradually degrades. Accordingly, the first-ply failure load level is taken to be 1580 N. The load drop, significant degradation in stiffness, and the initiation of large peak frequency bands at 2060 N indicate delamination failure in the main laminate.

Although the first-ply failure is due to delamination in $[(5/-5)_3]_s$, for the other angle-ply laminates, $[(+\theta/-\theta)_3]_s$, firstly intralaminar failure occurs. The results in Figure 7 show that with increasing θ angle in the specimens with $[(+\theta/-\theta)_3]_s$, layup configuration, the load level of delamination increases under anticlastic bending. The delamination failure in $[(5/-5)_3]_s$ occurs at 630 N; in the others, this value goes up to 1465 N in $[(15/-15)_3]_s$, and 2060 N in $[(30/-30)_3]_s$ laminate. In $[(45/-45)_3]_s$ laminate, delamination is not observed before the final failure at 3190 N (Figure 5).

The test results for unidirectional laminates with reinforcing strips are shown in Figure 8. The reinforcing strips significantly increase the strength of unidirectional laminates by postponing delamination failure. Unidirectional specimens with no strips fail under anticlastic bending at much lower load levels due to delamination as observed during the tests. Although the final failure strength of $[30_{12}]$ laminate with no strips is around 300 N, it increases to 700 N with reinforcing strips. For $[0_{12}]$ layup sequence, catastrophic failure occurs at 795 N as seen in Figure 8. Before this level, some AE signals are detected; however, energy levels are comparatively quite low and the AE signals do not form a consistent frequency band. For $[30_{12}]$ layup configuration, hits start to be recorded with high energy at 490 N, and different peak frequency levels are activated. Acoustic emission signals continue to be detected in the same frequency bands after the load is increased beyond this level. Cumulative curve shows a jump and increase with a high slope afterwards. The first-ply failure load level is accordingly taken as 490 N for $[30_{12}]$ specimen. For $[45_{12}]$ specimen, different frequency bands start to appear at about 7-mm displacement. However, energy levels of these signals are comparatively very low. Besides, there are no other indications that may be construed as first-ply failure: No load drop, no degradation in stiffness, no increase in the density of frequency bands, no significant and sustained increase in the slope of the cumulative curve, and no subsequent high-energy hits indicating progression of damage. Therefore, these hits do not correspond to a macro intralaminar damage mode. The large drop in the load level at the end of the test at 465 N associated with high-energy signal indicates the first-ply failure. In most of the unidirectional specimens, the first-ply failure load is the same as the ultimate load, where the specimen breaks apart. Because there is no load drop before the final failure, there is no indication of delamination failure.

Figure 9 shows the test results for a cross-ply laminate with $[90_3/0_3]_s$ layup sequence with no strips. Because there is no strip on the laminate, load drop at 1225 N cannot be attributed to separation of a strip from the plate. So based on the load–displacement curve, one may suppose that the first-ply failure of $[90_3/0_3]_s$ plate with no strips occurs with a load drop during displacement-controlled loading. Besides, the slope of the load–displacement curve, that is, the stiffness of the specimen, becomes lower after 1225 N. Successive signals with high-energy values and dense recording of peak frequency groups around 50 kHz and 150 kHz also confirm that the laminate sustains significant damage at this load level. A large increase in the slope of the cumulative count occurs at this load level. The load drop at 1225 N and subsequent significant decrease in stiffness indicate a large-scale delamination between the 0° and 90° plies as the first-ply failure mode. Previously recorded hits may be due to signals arising from some local matrix damage. Even though rubber bands are used between the specimen and the steel balls, the forces applied on the specimens are still localized. This may cause localized damage in the specimens at the points of application of the forces, resulting in signals detected by the AE instrument.

The load–displacement curve and AE recordings for $[90_3/0_3]_s$ laminate with strips are given in Figure 10. The reinforcing strips are very effective on the strength of this laminate. The level at which a significant load drop occurs increases with the strips as seen in Figures 9 and 10. This means that delamination of the laminate is delayed considerably with the reinforcing strips. However, the first-ply failure occurs at about the same load level. Signals with low energy values and different frequency groups are recorded before 1250 N, but this may be due to breaking of the adhesive or development of micro cracks. Activation of new frequency groups around 30 kHz and 340 kHz and high AE energy indicate the first-ply failure of the laminate at 1250 N. Slope of the cumulative-count curve also increases at this load level. Even though there is no large difference between the first-ply failure load levels of $[90_3/0_3]_s$ specimens with or without strips, apparently the mode of failure in this case is intralaminar matrix failure not delamination as opposed to the previous one. Significant degradation occurs in stiffness after delamination as seen in Figure 9. Intralaminar first-ply failure due to matrix damage, on the other hand, is not expected to cause significant stiffness degradation. In contrast to the case shown in Figure 9, no significant change in the load–displacement curve is

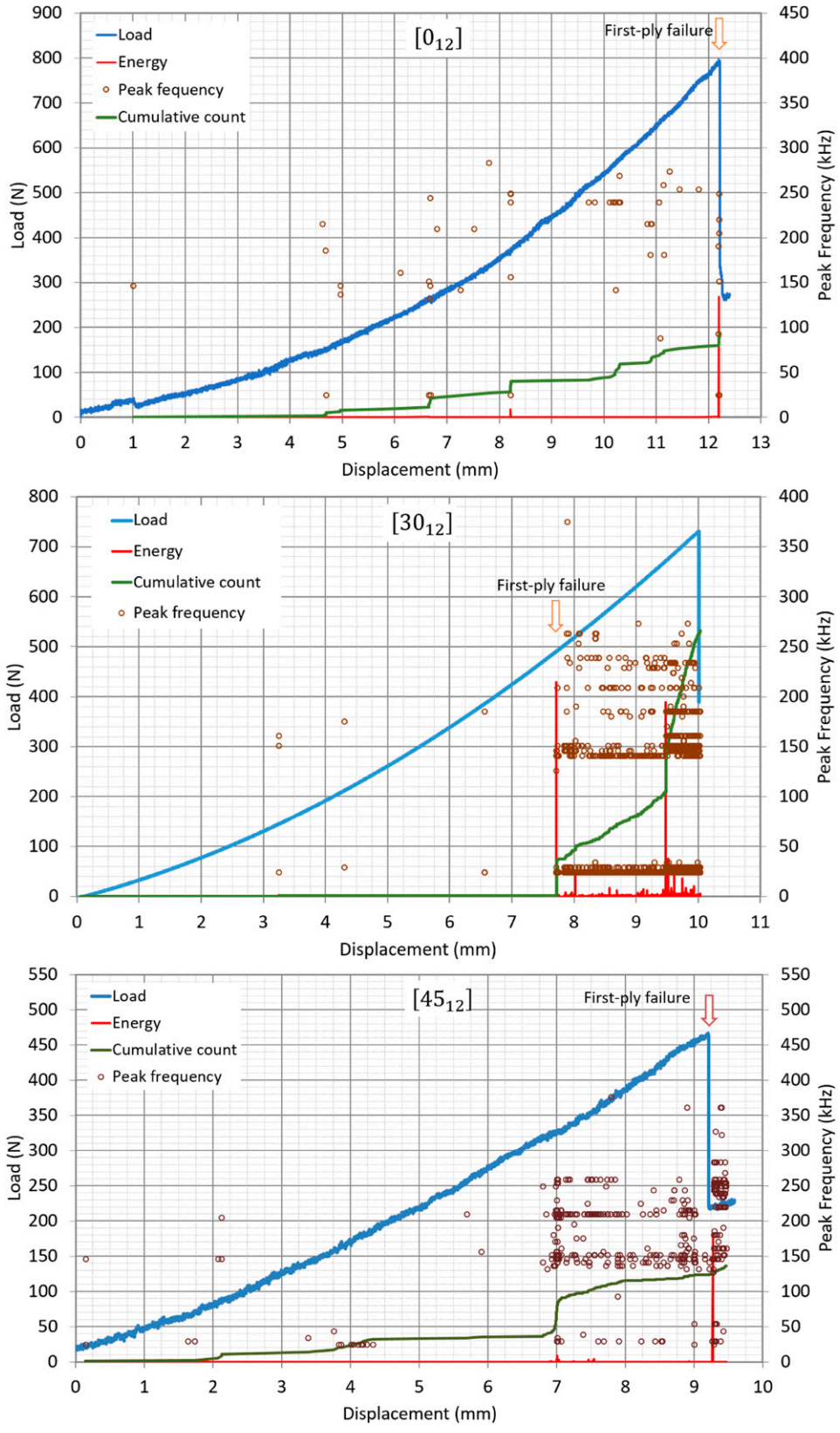

Figure 8. Test results for unidirectional laminates with reinforcing strips. For $[0_{12}]$ and $[45_{12}]$ specimens, the first-ply failure load is the same as the ultimate failure load. Although, there are previous AE signals, they have comparatively very low energy. In $[45_{12}]$ laminate, frequency bands form at about 7-mm displacement, but no subsequent high-energy signals and no significant and sustained increase in the slope of the cumulative curve are observed as opposed to $[30_{12}]$ specimen after it incurred first-ply failure at 490 N.

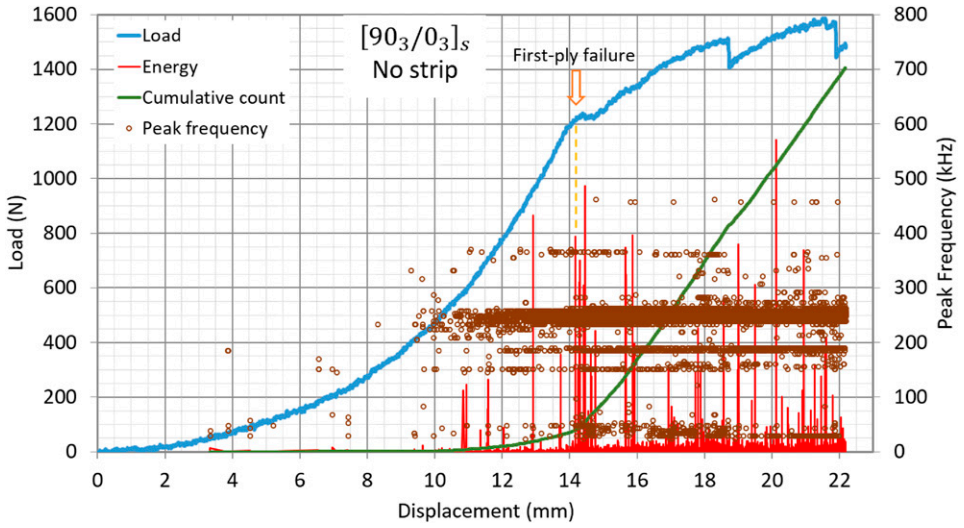

Figure 9. Test results for $[90_3/0_3]_s$ laminate with no strips.

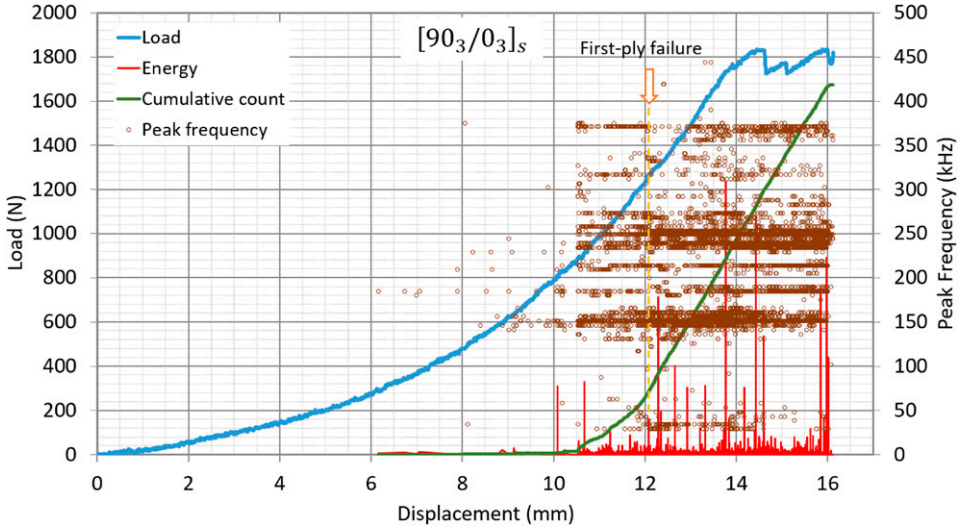

Figure 10. Test results for $[90_3/0_3]_s$ laminate with strips.

observed subsequently until 1830 N as seen in Figure 10. The load drop at this load level, significant loss in stiffness, and stopping in the recording of the frequency group around 30 kHz are attributed to a large-scale delamination between the 0° and 90° plies.

Figure 11 shows the load–displacement curve and AE readings for one of the specimens with $[(90/0)_3]_s$ layup configuration having strips. Comparison of Figures 10 and 11 shows that the ultimate strength is significantly higher than that of $[90_3/0_3]_s$. Specimens with $[(90/0)_3]_s$ layup sequence have higher ultimate strength by 41% on the average. The first-ply-failure load of this specimen can be taken as 1720 N. A relatively high-energy signal is recorded at that time. Subsequently, a slight drop occurs in the slope of the load–displacement curve and the cumulative-count curve shows an increase in slope. The previously recorded high-energy signals presumably indicate localized damage considering that no subsequent high-energy signal is recorded and the slope of the cumulative-count curve remains low. The load drop at 2450 N and subsequent decrease in stiffness indicate that the strips get partially seperated from the main laminate.

Comparison of the numerical and experimental results

Finite element analysis is carried out for each different test and the first-ply failure load is found using the chosen intralaminar failure criteria. Christensen–DeTeresa delamination criterion is also employed to check delamination

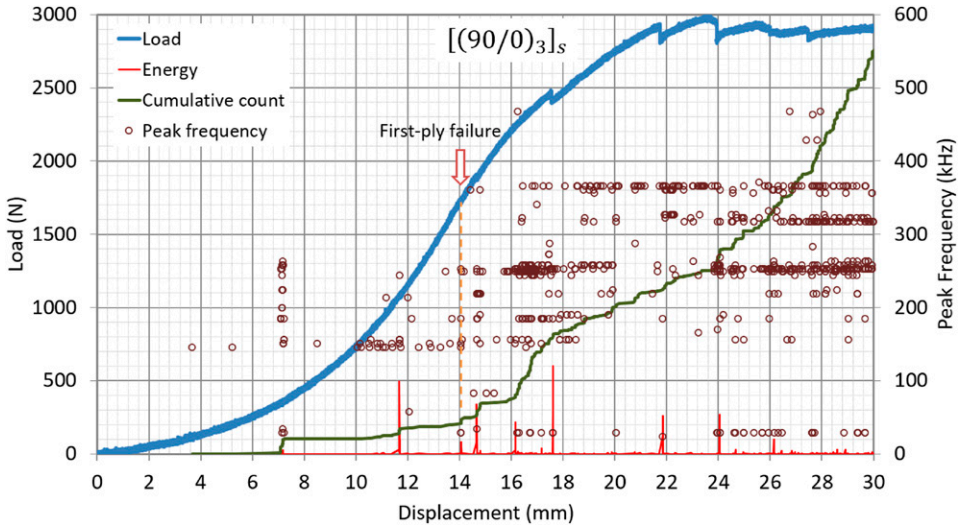

Figure 11. Test results for $[(90/0)_3]_s$ laminate with strips.

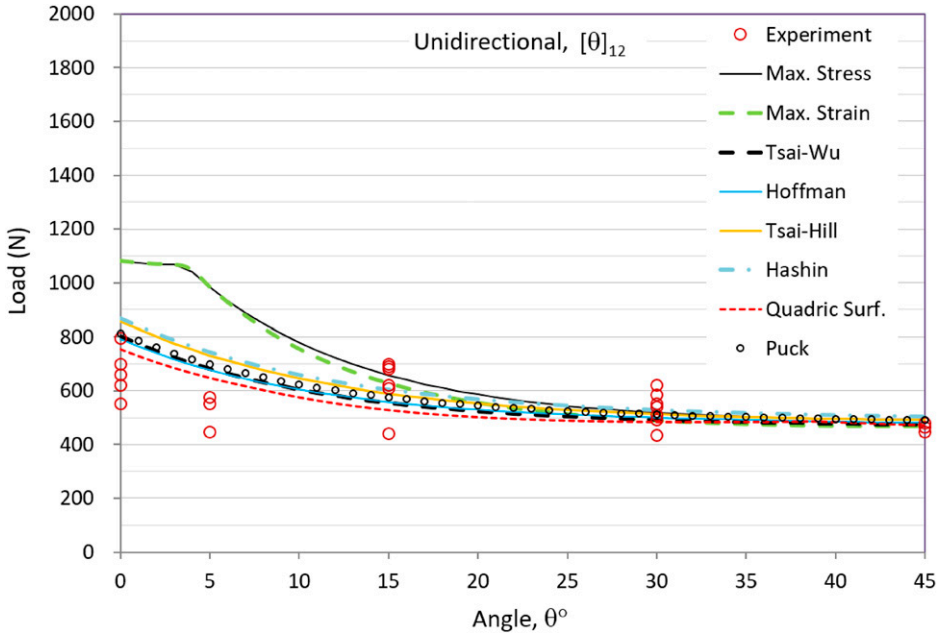

Figure 12. First-ply failure load versus orientation angle, θ, for the unidirectional laminates $[\theta_{12}]$.

failure. In none of the specimens, delamination is found to be critical according to the criterion.

Unidirectional laminates $[\theta_{12}]$. Figure 12 shows a comparison of the experimentally determined failure loads of unidirectional laminated plates, $[\theta_{12}]$, and the predictions obtained using the selected failure criteria. As seen in the figure, the maximum stress and maximum strain criteria predict a different trend from that of the others at small fiber orientation angles, θ. At larger angles, the predicted load levels become similar and after 20° the criteria estimate about the same values for the failure loads. Except the maximum stress and maximum strain, the failure criteria predict a decreasing trend for the strength with the increase in the orientation angle, θ. The experimental results indicate, however, a decrease in strength for $\theta = 5^{\circ}$, then increase at 15°, after that a continual decrease until $\theta = 45^{\circ}$. The experimental scatter in the strength of the unidirectional specimens is relatively large. This may be attributed to the sensitivity of the matrix dominated transverse strength to manufacturing defects, which has much more bearing on unidirectional laminates.

Table 4. The mean, μ, and the coefficient of variation, CoV (%) of the measured values of the first-ply failure load, F, for the unidirectional specimens, $[\theta_{12}]$, and the percentage error in the predictions of the failure criteria. F_u is the mean value of the measured ultimate strength.

	Measured F		F_u (N)	Error (%) $(100*(F_{pred} - F_{exp})/F_{exp})$							
Lay-up	μ	CoV(%)	μ	Max. Stress	Max. Strain	Tsai–Wu	Tsai–Hill	Hoffman	Hashin	Quad. Surf	Puck
$[0_{12}]$	665	13.7	665	62.5	62.5	20.7	28.9	19.2	30.4	13.4	22.5
$[5_{12}]$	523	13.2	523	88.0	87.8	30.5	39.7	29.5	41.8	23.8	33.5
$[15_{12}]$	623	15.6	977	5.5	0.6	−11.0	−5.4	−10.5	−3.3	−15.3	−7.7
$[30_{12}]$	533	11.5	585	−2.7	−8.4	−7.8	−3.7	−6.2	−1.0	−9.2	−4.0
$[45_{12}]$	463	3.8	463	6.5	1.1	2.5	6.1	4.0	8.7	1.7	5.9
Average error (%)				33.0	32.1	14.5	16.8	13.9	17.0	12.7	14.7

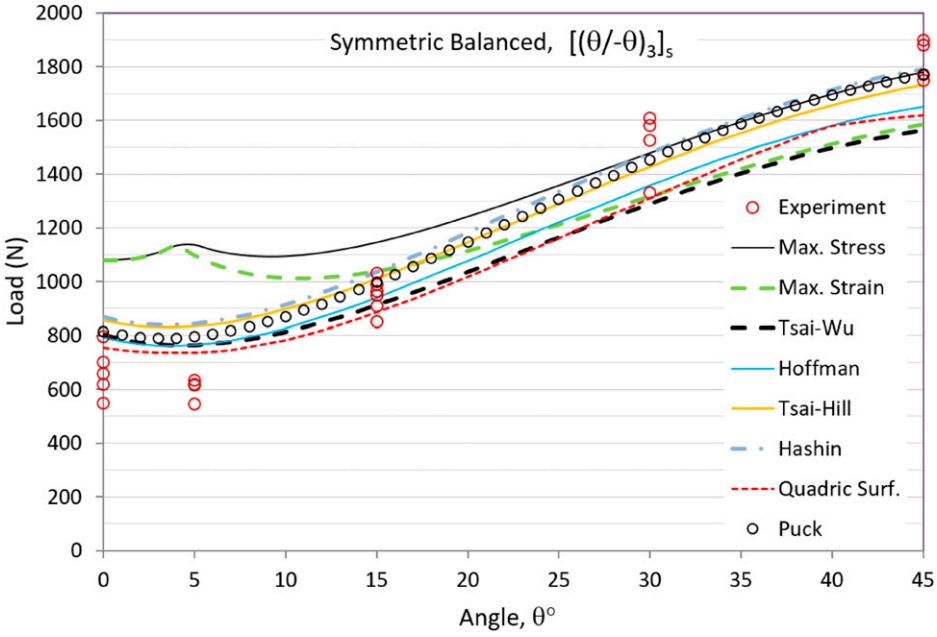

Figure 13. First-ply failure load versus orientation angle, θ, graph for the symmetric angle-ply laminates $[(+\theta/-\theta)_3]_s$.

The stress state in material coordinates at the node where the failure index is equal to 1.0 according to the maximum stress criterion is calculated as $\sigma_1 = -320.6$, $\sigma_2 = 63.9$, $\sigma_3 = -0.8$, $\sigma_{12} = 8.5$, $\sigma_{23} = 0.7$, and $\sigma_{13} = -2.1$ MPa for $[45_{12}]$ laminate. Recognizing that $\sigma_2 = Y_t$, matrix failure under tension occurs at the most critical location. The other modes of failure are far less critical. Similarly, for the other criteria, $\sigma_2 \cong Y_t$ at the critical locations. This is considered to be the reason for the similar values of failure load predicted by different criteria as seen in Figure 12. On the other hand, for $[5_{12}]$ laminate, where the discrepancy in the predicted failure load levels is high, the stress state at the critical location according to the maximum stress criterion is calculated as $\sigma_1 = -49.2$, $\sigma_2 = 63.9$, $\sigma_3 = -2.2$, $\sigma_{12} = -100.9$, $\sigma_{23} = -1.0$, and $\sigma_{13} = 5.8$ MPa. Failure occurs, because $\sigma_2 = Y_t$ according to the maximum stress criterion, but the shear stress is close to its strength limit (Table 2). In these cases, interaction between different failure modes is possible. Tsai–Wu is a failure criterion that accounts for interaction. The stress state at the critical location according to Tsai–Wu criterion is calculated as $\sigma_1 = 29.7$, $\sigma_2 = 43.9$, $\sigma_3 = -1.8$, $\sigma_{12} = -72.8$, $\sigma_{23} = -1.2$, and $\sigma_{13} = -3.1$ MPa. Tsai–Wu predicts a much lower failure load compared to the maximum stress criterion as seen in the figure and it is closer to the experimental result.

Table 4 presents the experimental results for the failure loads of the unidirectional specimens and the percentage errors in the predictions of the failure criteria. As seen in

Table 5. The mean, μ, and the coefficient of variation, CoV (%) of the measured values of the first-ply failure load, F, for the symmetric angle-ply specimens, $[(+\theta/-\theta)_3]_s$, and the percentage error in the first-ply failure predictions of the failure criteria. F_u is the mean value of the measured ultimate strength.

	Measured F		F_u (N)	Error (%) $(100*(F_{pred} - F_{exp})/F_{exp})$							
Lay-up	μ	CoV(%)	μ	Max. Stress	Max. Strain	Tsai–Wu	Tsai–Hill	Hoffman	Hashin	Quad. Surf	Puck
$[(5/-5)_3]_s$	604	6.6	608	88.1	81.8	26.7	38.1	26.8	39.8	22.0	32.0
$[(15/-15)_3]_s$	949	6.6	1528	20.6	9.5	−3.8	6.4	−0.9	9.2	−6.7	5.1
$[(30/-30)_3]_s$	1511	8.3	2219	−2.2	−12.8	−14.7	−5.5	−10.1	−2.2	−13.3	−3.8
$[(45/-45)_3]_s$	1825	4.2	3303	−2.6	−13.1	−14.3	−5.1	−9.5	−1.9	−11.2	−3.1
Average error (%)				35.2	35.9	16.0	16.8	13.3	16.7	13.3	13.3

Table 6. Mean values of the experimental results and percentages of error in the first-ply failure predictions of the failure criteria for cross-ply laminates. F_u is the mean value of the measured ultimate strength.

	Measured F		F_u (N)	Error (%) $(100*(F_{pred} - F_{exp})/F_{exp})$							
Lay-up	μ	CoV(%)	μ	Max. Stress	Max. Strain	Tsai–Wu	Tsai–Hill	Hoffman	Hashin	Quad. Surf	Puck
$[(90/0)_3]_s$	1793	2.9	2893	−32.5	−32.5	−35.4	−38.0	−38.4	−35.0	−40.7	−37.5
$[90_3/0_3]_s$	1367	9.1	2053	−10.6	−10.6	−15.8	−19.9	−20.5	−15.3	−23.2	−19.0

the tables, the largest discrepancies between the experimental results and the predictions occur for $[0_{12}]$ and $[5_{12}]$ configurations. Over-prediction for these specimens is not attributed to premature separation of the strips in the experiments. As seen in Figure 8, these specimens fail suddenly at the highest load without any indication of prior damage. Among the failure criteria, the maximum stress and maximum strain criteria yield the worst predictions with an error up to 88%. The quadric surfaces criterion returns relatively good predictions with an average error of 12.7%. Hoffman, Tsai–Wu, and Puck criteria also yield good results. The table also provides the ultimate loads. Except for the specimens having $[15_{12}]$ and $[30_{12}]$ layup sequences, the first-ply failure load and the ultimate load are the same.

Symmetric angle-ply laminates $[(+\theta/-\theta)_3]_s$. Figure 13 shows a comparison of the experimentally determined first-ply failure loads of symmetric angle-ply specimens, $[(+\theta/-\theta)_3]_s$, and the predictions obtained using the selected failure criteria. Table 5 presents the experimental results and the percentage errors in the predictions of the selected failure criteria. According to the experiments, the strength of the material decreases to $\theta = 5^\circ$ and then increases continuously. The highest strength is obtained for $[(+45/-45)_3]_s$, while $[(+5/-5)_3]_s$ has the lowest strength. The scatter in the experimental results is lower compared to the unidirectional specimen results. Except for the maximum stress and maximum strain criteria, the failure criteria correctly estimate the failure trend; that is, its decrease to $\theta = 5^\circ$ and then increase. Since the examination of the load–displacement curve and acoustic emission recordings of the specimen with $[(5/-5)_3]_s$ layup sequence revealed that this specimen first failed due to delamination, the decrease of intralaminar strength for $\theta = 5^\circ$ is not a conclusive finding. However, considering that most of the failure criteria predict a decreasing trend up to $\theta = 5^\circ$ and according to the delamination criterion, delamination failure is less critical, this conclusion can be tentatively accepted. The intralaminar failure criteria overestimate the strength for $\theta = 0^\circ$ and $\theta = 5^\circ$ while they underestimate for $\theta = 30^\circ$ and $\theta = 45^\circ$ Puck, quadric surfaces, and Hoffman criteria yield better predictions with an average error of 13.3%.

Cross-ply layup sequences. The experimental results for $[(90/0)_3]_s$ and $[90_3/0_3]_s$ layup sequences and percentages of error in the predictions are tabulated in Table 6. Experiments show that the first-ply failure strength of $[(90/0)_3]_s$ laminate is considerably higher than that of $[90_3/0_3]_s$ laminate. In contrast, the predictions of the failure criteria do not indicate significant difference in strength for the two configurations. They considerably underestimate the strength of $[(90/0)_3]_s$ laminates.

Conclusions

In this study, failure behavior of laminated composite plates made of AS4/8552 prepregs under anticlastic bending is investigated. A fixture is designed to achieve

anticlastic loading. Reinforcing strips are glued to the edges of the specimens to avoid premature failure by delamination.

First-ply failure rarely occurs in composite parts in the form of sudden and total failure of a layer unlike coupon tests, but typically occurs at a region where stresses are locally high. For this reason, initial damage may occur without appreciable degradation in stiffness like decrease in the slope of the load–displacement curve. In many cases including even the coupon tests, it is not possible to determine the first-ply failure load by just examining the load–displacement curve without the help of other indicators like AE signals. In this study, the first-ply failure load is determined using acoustic emission monitoring (AEM) besides change in the slope of force–displacement curve. Damage in composite parts may occur locally at low load levels due to a manufacturing defect, however, this cannot be considered as first-ply failure even though it generates an acoustic signal. If damage initiates at a given load level and progresses with an increase in load, then it is considered as first-ply failure. In light of this definition, in order to differentiate false signals, the following criteria are proposed in this study as indications of ply failure based on acoustic signals: A high-energy signal together with formation of frequency bands, considerable change in the slope of cumulative-count curve, and subsequently recorded high-energy signals after detecting a high-energy signal.

A finite element model is developed to carry out the structural analysis of the specimen under anticlastic bending. Selected failure criteria are then employed to predict the failure load. For unidirectional laminates, $[\theta_{12}]$, the best correlation is obtained with Tsai–Wu, Hoffman, Puck, and quadric surfaces criteria. All the criteria significantly overestimate the strengths of $[0_{12}]$ and $[5_{12}]$ configurations except quadric surfaces. Maximum stress and maximum strain criteria predict the strength of $[5_{12}]$ higher than that of $[0_{12}]$, while the others predict the highest strength for $[0_{12}]$, then continuously decreasing strength up to 45°. For symmetric angle-ply laminates, $[(+\theta/-\theta)_3]_s$, maximum stress and maximum strain estimate increasing strength up to 6°, while the others estimate first a decrease, after that continuous increase up to 45°. The experimental results confirm the latter predicted trend. Puck, quadric surfaces, and Hoffman criteria show the best correlation for symmetric angle-ply laminates based on average error. For cross-ply specimens, while the failure criteria predict about the same first-ply strength for $[(90/0)_3]_s$ and $[90_3/0_3]_s$, the strength of $[(90/0)_3]_s$ is found to be much larger in the experiments.

Acknowledgements

The authors would also like to thank to Istanbul Development Agency, which supported the development of the infrastructure of Composites Laboratory at Bogazici University under project code ISTKA/BIL/2012/58, and Bogazici University Research Fund, which supported the development of the infrastructure of Mechanical Testing Laboratory under project code 14A06S3.

Declaration of conflicting interests

The author(s) declared no potential conflicts of interest with respect to the research, authorship, and/or publication of this article.

Funding

The author(s) disclosed receipt of the following financial support for the research, authorship, and/or publication of this article: This paper is based on the work supported by Bogazici University Research Fund with grant numbers 13A06P5 and 15A06D3 and Istanbul Kalkinma Ajansi with grant number ISTKA/BIL/2012/58.

ORCID iDs

Yakup O. Alpay https://orcid.org/0000-0001-8038-7994
Fatih E Oz https://orcid.org/0000-0002-3532-1205
Fazil O Sonmez https://orcid.org/0000-0003-4065-8862

References

1. Soden PD, Hinton MJ and Kaddour AS. A comparison of the predictive capabilities of current failure theories for composite laminates. *Compos Sci Technol* 1998; 58(7): 1225–1254.
2. Hinton MJ and Soden PD. Predicting failure in composite laminates: The background to the exercise. *Compos Sci Technol* 1998; 58(7): 1001–1010.
3. Soden PD, Hinton MJ and Kaddour AS. Biaxial test results for strength and deformation of a range of E-glass and carbon fibre reinforced composite laminates: Failure exercise benchmark data. *Compos Sci Technol* 2002; 62(12–13 SPECIAL ISSUE): 1489–1514.
4. Puck A and Schürmann H. Failure analysis of FRP laminates by means of physically based phenomenological models. *Compos Sci Technol* 2002; 62(12–13 SPECIAL ISSUE): 1633–1662.
5. Hinton MMJ, Kaddour AS and Soden PD. A comparison of the predictive capabilities of current failure theories for composite laminates, judged against experimental evidence. *Compos Sci Technol* 2002; 62(12–13 SPECIAL ISSUE): 1725–1797.
6. Kaddour AS and Hinton MJ. Benchmarking of triaxial failure criteria for composite laminates: Comparison between models of 'Part (A)' of 'WWFE-II'. *J Compos Mater* 2012; 46(19–20): 2595–2634.
7. Kaddour AS, Hinton MJ, Smith PA, et al. A comparison between the predictive capability of matrix cracking, damage and failure criteria for fibre reinforced composite laminates: Part A of the third world-wide failure exercise. *J Compos Mater* 2013; 47(20–21): 2749–2779.
8. Kaddour AS and Hinton MJ. Maturity of 3D failure criteria for fibre-reinforced composites: Comparison between theories and experiments: Part B of WWFE-II. *J Compos Mater* 2013; 47(6–7): 925–966.
9. Shahabi E and Forouzan MR. A damage mechanics based failure criterion for fiber reinforced polymers. *Composites Sci Tech* 2017; 140: 23–29.

10. Irhirane H, Echaabi J, Aboussaleh M, et al. Matrix and fibre stiffness degradation of a quasi-isotrope graphite epoxy laminate under flexural bending test. *J Reinforced Plastics Composites* 2009; 28(2): 201–223.
11. Meng M, Le HR, Rizvi MJ, et al. 3D FEA modelling of laminated composites in bending and their failure mechanisms. *Compos Structures* 2015; 119: 693–708.
12. Koc M, Sonmez FO, Ersoy N, et al. Failure behavior of composite laminates under four-point bending. *J Compos Mater* 2016; 50(26): 3679–3697.
13. Kim Y, Davalos JF and Barbero EJ. Progressive failure analysis of laminated composite beams. *J Compos Mater* 1996; 30(5): 536–560.
14. Feraboli P and Kedward KT. Four-point bend interlaminar shear testing of uni- and multi-directional carbon/epoxy composite systems. *Composites A: Appl Sci Manufacturing* 2003; 34(12): 1265–1271.
15. Huang Z-M. Modeling and characterization of bending strength of braided fabric reinforced laminates. *J Compos Mater* 2002; 36(22): 2537–2566.
16. Hara E, Yokozeki T, Hatta H, et al. Comparison of out-of-plane tensile strengths of aligned CFRP obtained by 3-point bending and direct loading tests. *Composites Part A: Appl Sci Manufacturing* 2012; 43(11): 1828–1836.
17. Greif R and Chapon E. Investigation of successive failure modes in graphite/epoxy laminated composite beams. *J Reinforced Plastics Composites* 1993; 12: 602–621.
18. Huang Z.-M. Failure analysis of laminated structures by FEM based on nonlinear constitutive relationship. *Compos Structures* 2007; 77(3): 270–279.
19. Echaabi J, Trochu F, Pham XT, et al. Theoretical and experimental investigation of failure and damage progression of graphite-epoxy composites in flexural bending test. *J Reinforced Plastics Composites* 1996; 15(7): 740–755.
20. Huybrechts S, Maji A, Lao J, et al. Validation of the quadratic composite failure criteria with out-of-plane shear terms. *J Compos Mater* 2002; 36(15): 1879–1888.
21. Irhirane EH, Abousaleh M, Echaabi J, et al. Modeling and simulation of the failure and stiffness degradation of a graphite epoxy in a three point bending test. *J Eng Mater Technol Trans ASME* 2010; 132(3): 0310131–0310138.
22. Vargas G and Mujika F. Determination of in-plane shear strength of unidirectional composite materials using the off-axis three-point flexure and off-axis tensile tests. *J Compos Mater* 2010; 44(21): 2487–2507.
23. Li X, Yan Y, Tan Y, et al. Experimental and numerical investigations of the interlaminar shear properties of carbon/carbon composites. *J Appl Polym Sci* 2017; 134(23).
24. Chen AS, Matthews FL and Sims GD. The effect of support conditions on the performance of CFRP plates subjected to bi-axial flexure. *Compos Sci Technol* 1998; 58(3–4): 613–621.
25. Günel M and Kayran A. Non-linear progressive failure analysis of open-hole composite laminates under combined loading. *J Sandw Struct Mater* 2013; 15(3): 309–339.
26. Padhi G. S., Shenoi R. A., Moy S. S. J., et al. Progressive failure and ultimate collapse of laminated composite plates in bending. *Compos Structures* 1997; 40(3–4): 277–291.
27. Farshad M, Wildenberg MW and Flüeler P. Determination of shear modulus and poisson's ratio of polymers and foams by the anticlastic plate-bending method. *Mater Struct* 1997; 30(200): 377–382.
28. Farshad M and Flüeler P. Investigation of mode III fracture toughness using an anti-clastic plate bending method. *Eng Fract Mech* 1998; 60(5–6): 597–603.
29. Makeev A, Seon G, Cline J, et al. In quest of methods for measuring 3D mechanical properties of composites. *Composites Sci Tech* 2014; 100: 105–112.
30. Podczeck F. The determination of fracture mechanics properties of pharmaceutical materials in mode III loading using an anti-clastic plate bending method. *Int J Pharm* 2001; 227(1–2): 39–46.
31. Elmalich D and Rabinovitch O. Twist in soft-core sandwich plates. *Jnl Sandwich Structures Mater* 2014; 16(6): 577–613.
32. Goodsell J, Pagano NJ and Kravchenko O. Interlaminar stresses in composite laminates subjected to anticlastic bending deformation. *ASME J Appl Mech* 2013; 80: 1–7.
33. Yeh H. Quadric surfaces criterion for composite materials. *J Reinforced Plastics Composites* 2003; 22(6): 517–532.
34. *Hexcel AS4/8552 Product Data Sheet*. Available at: https://www.hexcel.com/user_area/content_media/raw/HexPly_8552_us_DataSheet.pdf (Last accessed July 2022).
35. Lopes CS, Seresta O, Coquet Y, et al. Low-velocity impact damage on dispersed stacking sequence laminates. Part I: Experiments. *Composites Sci Tech* 2009; 69: 926–936.
36. *HexPly 8552 Epoxy Matrix (180°C Curing Matrix), Product Data*, Hexcel Composites. 2008.
37. AEWin Software. *User's Reference Manual, Rev.4*. Princeton Junction, NJ, USA: MISTRAS Group Inc., Products & Systems Division, 2011.
38. Oz FE, Ersoy N and Lomov SV. Do high frequency acoustic emission events always represent fibre failure in CFRP laminates? *Composites Part A: Appl Sci Manufacturing* 2017; 103: 230–235.
39. Oz FE, Ersoy N, Mehdikhani M, et al. Multi-instrument in-situ damage monitoring in quasi-isotropic CFRP laminates under tension. *Compos Structures* 2018; 196: 163–180.
40. Oz FE, Ahmadvashaghbash S. and Ersoy N. Damage mode identification in transverse crack tension specimens using acoustic emission and correlation with finite element progressive damage model. *Composites B: Eng* 2019; 165: 84–95.
41. Gutkin R, Green CJ, Vangrattanachai S, et al. On acoustic emission for failure investigation in CFRP: Pattern recognition and peak frequency analyses. *Mech Syst Signal Process* 2011; 25(4): 1393–1407.
42. de Groot PJ, Wijnen PAM and Janssen RBF. Real-time frequency determination of acoustic emission for different fracture mechanisms in carbon/epoxy composites. *Composites Sci Tech* 1995; 55(4): 405–412.
43. Aramugam V, Kumar SB, Santulli C, et al. Effect of fiber orientation in uni-directional glass epoxy laminate using acoustic emission monitoring. *Acta Metallurgica Sinica* 2011; 24: 351–364.
44. Kam TY and Lai FM. Experimental and theoretical predictions of first-ply failure strength of laminated composite plates. *Int J Sol Structures* 1999; 36(16): 2379–2395.
45. Baker C, Morscher GN, Pujar VV, et al. Transverse cracking in carbon fiber reinforced polymer composites: Modal acoustic

emission and peak frequency analysis. *Composites Sci Tech* 2015; 116: 26–32.
46. Uzal A, Sonmez FO, Oz FE, et al. A composite sandwich plate with a novel core design. *Compos Structures* 2018; 193: 198–211.
47. Oz F. E., Calik E. and Ersoy N. Finite element analysis and acoustic emission monitoring of progressive failure of corrugated core composite structures. *Compos Structures* 2020; 253. 112775.
48. Tabrizi I. E., Oz F. E., Zanjani J. S. M., et al. Failure Sequence Determination in Sandwich Structures Using Concurrent Acoustic Emission Monitoring and Postmortem Thermography. *Mech Mater* 2021; 164: 104113.
49. Christensen RM and DeTeresa SJ. Delamination failure investigation for out-of-plane loading in laminates. *J Compos Mater* 2004; 38(24): 2231–2238.
50. Clarkson E. *Hexcel 8552 AS4 Unidirectional Prepreg Qualification Statistical Report*. National Institute for Aviation Research, Wichita State University.
51. Perogamvros NG and Lampeas GN. Experimental and numerical investigation of AS4/8552 interlaminar shear strength under impact loading conditions. *J Compos Mater* 2016; 50(19): 2669–2685.
52. Jones RM. *Mechanics of Composite Materials*. 2nd ed. Philadelphia: Taylor & Francis, 1999.
53. Hashin Z. Failure criteria for unidirectional fiber composites. *J Appl Mech* 1980; 47: 329–334.
54. Tsai SW and Wu EM. A general theory of strength for anisotropic materials. *J Compos Mater* 1971; 5: 58–80.
55. Puck A and Schürmann H. Failure analysis of FRP laminates by means of physically based phenomenological models. *Compos Sci Technol* 1998; 58(7): 1045–1067.
56. Puck A, Kopp J and Knops M. Guidelines for the determination of the parameters in Puck's action plane strength criterion. *Composites Sci Tech* 2002; 62: 371–378.
57. Hoffman O. The brittle strength of orthotropic materials. *J Compos Mater* 1967; 1(2): 200–206.
58. Yeh H-L. Quadric Surfaces Criterion for Composite Materials. *J Reinforced Plastics Composites* 2003; 22(6): 517–532.
59. ANSYS Help, Version: 2020.